RSC Advances

ROYAL SOCIETY OF CHEMISTRY

www.rsc.org/advances

Effects of morphology, surface area, and defect content on the photocatalytic dye degradation performance of ZnO nanostructures

Natalia Morales Flores[a], Umapada Pal[b*], Reina Galeazzi[a] and Alberto Sandoval[b]

Abstract

ZnO nanostructures of different morphologies were fabricated through ultrasound-assisted hydrolysis of zinc acetate at room temperature, by controlling the pH of the reaction mixture. It has been observed that the pH of the reaction solution affects both the morphology and defect content of the nanostructures. To study the effects of morphology and other parameters like specific surface area, defect content, and surface contamination on photocatalytic activity, both the as-grown and air-annealed nanostructures were tested for methylene blue (MB) degradation under UV light. While all the above mention parameters have seen to affect the photocatalytic performance of ZnO nanostructures, specific surface area, defect content, and carbon contamination at the surface have seen to be the most important parameters, which should be controlled for their application in photocatalysis. Therefore, for photocatalytic applications of ZnO nanostructures, not only their morphology or the specific surface area are important, care should be taken to control their defect contents and surface contaminants.

1. INTRODUCTION

Metal oxide nanostructures such as titanium dioxide (TiO_2), zinc oxide (ZnO), iron oxide (Fe_2O_3), and zirconium oxide (ZrO_2), have been utilized extensively as photocatalyst for the degradation of organic pollutants in water and air.[1-3] Although TiO_2 has been the most utilized metal oxide photocatalysts for environmental applications, ZnO has been suggested as an alternative low cost photocatalyst[4] for the degradation of organic molecules in aqueous solution.[5] The interests of utilizing ZnO as photocatalyst alternative to TiO_2 lie mainly in its similar electronic properties[6] and higher photoefficiency than TiO_2.[7,8]

Recently, ZnO nanoparticles have been utilized as photocatalyst for the degradation of organic dyes such as methylene blue, methyl red, and methyl orange.[9-14] While the photocatalytic activity of ZnO nanostructures depends strongly on their sizes, basically due to enhanced specific surface area of smaller structures, the shape of the nanostructures has also seen to affect their photocatalytic performance strongly.[15,16]

It has been demonstrated that ZnO can work as a better photocatalyst than TiO_2 in the degradation of organic pollutants including dyes.[4,17] For example, Akyol et al.[18] have studied the photocatalytic decolorization of an azo-reactive textile dye Remazol red (RR), using various metal oxide semiconductor catalysts, finding ZnO powder as the most active catalyst, exhibiting activity even higher than TiO_2. On the other hand, Dindar and Icli[4] found ZnO as active as TiO_2 for the photocatalytic degradation of phenol under concentrated sunlight. Lee et al.[19] have reported the Photocatalytic degradation of total organic carbon (TOC) from aqueous phenol solution using both ZnO and TiO_2 nanopowders, finding about 1.6 fold higher degradation rate for ZnO nanopowder than Degussa P-25 (commercial TiO_2 nanopowder from Degussa, generally used as a standard photocatalyst). While Wang et al.[20] have reported an enhanced photocatalytic activity of nano-sized ZnO/SnO_2 mixed oxide for methyl orange degradation after calcination at 500 $^{\circ}$C for 10 h, Chakrabarti and Dutta[21] have studied the photodegradation of methylene blue and eosin Y dyes in aqueous suspensions of ZnO, demonstrating a higher degradation rate of MB at similar experimental conditions. The photocatalytic degradation of acid yellow 36 in aqueous media using zinc oxide as catalyst has also been studied by Khezrianjoo and Revanasiddappa,[22] monitoring the effects of solution pH, and catalyst loading. While the particle size, phase composition, and specific surface area are the parameters known to affect the photocatalyic behavior of TiO_2 nanostructures,[23-25] the same factors along with the geometrical shape[12,26] have seen to affect the photocatalytic performance of ZnO nanostructures strongly.

On the other hand, ZnO nanostructures doped with different metals have been utilized for photocatalytic degradation of organic pollutants. For example, Kong et al.[10] have studied the photodegradation of MB using Ta-doped ZnO nanoparticles, finding excellent performance for 1% Ta-doped ZnO after annealing at 700°C. The better photocatalyic performance of ZnO:Ta nanoparticles was attributed to a competitive trade-off among the

crystallinity, surface hydroxyl groups, and specific surface area of the nanostructures. Height et al.[27] have used Ag-ZnO catalysts for UV-photodegradation of MB, finding 3.0 atom % Ag loading as optimum. Ullah and Dutta[28] have studied the photodegradation of organic dyes using Mn-doped ZnO nanoparticles, finding their MB photodegradation efficiency significantly higher than undoped ZnO and TiO_2. Wang et al.[29] have also observed enhanced photocatalytic activity of ZnO nanocrystals for MB degradation on Ag doping. Apart from a small shift of band gap energy on metal ion doping, which also shifts the photo-response peak of ZnO nanostructures towards lower or higher energy (wavelength) side, their enhanced photocatalytic behavior has been attributed to the change of surface properties such as an increased O vacancies, higher crystalline defects, and increased specific surface area on doping. For example, incorporation of silver ions in higher quantity increases the lattice defects in the ZnO nanostructures, enhancing their photocatalytic activity.[29] Though ZnO nanostructures of different morphologies and different metal doping have been utilized for photocatalytic degradation of different organic pollutants, and the effects of nanostructure morphology and doping (nature and concentration of dopants) have been studied by several research groups, the effects of morphology on the photocatalytic behaviors of ZnO nanostructures are not yet clear. In fact, the photocatalytic behavior of ZnO nanostructures depends also on several other factors.

In the present article, we present the photocatalytic behavior ZnO nanostructures of different morphologies synthesized by ultrasound-assisted hydrolysis of zinc acetate at room temperature for the degradation of methylene blue (MB) in aqueous solution. The ZnO nanostructures were prepared by low-power sonication of aqueous zinc acetate at different pH values of the reaction mixture in presence of EDTA, and characterized using scanning electron microscopy (SEM), X-ray diffraction (XRD), diffuse reflectance spectroscopy (DRS), and photoluminescence (PL) techniques. The efficiency of MB photodegradation of the as-synthesized and air-annealed nanostructures under UV radiation has been studied. Apart from presenting the effect of pH of the reaction solution on the morphology evolution of ZnO nanostructures, effects of morphology, specific surface area, defect content, and carbon impurity on their photocatalytic behavior have been discussed.

2. EXPERIMENTS AND METHODS

ZnO nanostructures of different morphologies were synthesized by the sonochemical technique using ethylenediaminetetraacetic acid (EDTA) as the chelating agent. Zinc acetate dihydrate [$Zn(CH_3COO)_2•2H_2O$, Baker, 99.9%], EDTA [($C_{10}H_{16}N_2O_8$), Sigma Aldrich, 99.4%], and ammonium hydroxide [NH_4OH, EMD, 29%], were used as received for preparing the precursor solutions in deionized water (ρ >18.2 M Ω-cm). A solution was prepared by dissolving 3 g of $Zn(CH_3COO)_2•2H_2O$ and 0.5 g of EDTA in 200 mL of deionized (DI) water at room temperature under vigorous magnetic stirring. After about 20 minutes of agitation, an appropriate amount of NH_4OH was slowly added into the previous solution until its pH reaches to the desired value. The variation of solution pH was monitored by a digital pH-meter (conductronic) during the drop-wise addition of NH_4OH. Several reaction solutions were prepared with different final pH values in between 7.5 and 10. After about 15 minutes of magnetic stirring, each of the solutions was subjected to ultrasonic treatment for 3 h under Ar bubbling. The ultrasonic irradiation was imparted by a T-horn of an ultrasonic processor (UP400S, Hielscher, 400 Watt, and 24 kHz) at 40 W dissipating power. Finally, the obtained product was separated by centrifuging, washed several times with ethanol (8000 rpm for 10 minutes), and dried at 70 °C for 6 h in a muffle furnace, obtaining powder samples.

All the powder samples were analyzed by X-ray diffraction (XRD) (Bruker AXS D8 Discover diffractometer operating at 40 kV and 40 mA with monochromatic CuKα (λ=1.5406 Å) radiation), field emission high resolution scanning electron microscopy (FE-HRSEM) (Zeiss, Auriga 3916), diffuse reflectance spectroscopy (DRS) in UV-Vis spectral range, and room temperature photoluminescence (PL) techniques. For the determination of specific surface area of the samples, their nitrogen adsorption-desorption isotherms at 77 K were recorded in a Belsorp-Mini II (BEL Japan, Inc.) analyzer. The samples were degassed at 250 °C for 5 h in vacuum prior to the measurements.

A UV–Vis–NIR spectrophotometer (UV-3101PC, Shimadzu) was utilized to monitor the photocatalytic behavior of the ZnO nanostructures. The photocatalytic tests were performed in an aqueous solution using methylene blue (MB) ($C_{16}H_{18}ClN_3S•3H_2O$, Sigma-Aldrich) as a test contaminant. The photochemical reactor used in the present study was a cylindrical

jacketed glass mini-reactor of 500 mL capacity with 50 mm internal diameter and about 120 mm of height. The room temperature MB photodegradation rate of the catalysts was monitored by dispersing 100 mg of powder ZnO sample in 100 mL of water containing MB in 10 ppm concentration. The catalyst containing reaction mixture was illuminated by a 10W ultraviolet LED lamp (model JX-10UV9X1B365) with predominant emission at λ = 365 nm. The lamp was placed at the top of the reactor, about 12.5 cm above the test solution surface. The temperature of the reaction mixture was maintained fixed at 25 ^{o}C by circulating cold water through the jacket of the reactor. Oxygen was bubbled through the reaction solution under UV illumination. The MB concentration in the reaction mixture was monitored by the computer-controlled spectrophotometer at regular time intervals, withdrawing each time about 3.5 mL of the solution (aliquot) from the reactor. To separate the dispersed catalyst from the aliquot, a reusable syringe filter holders (z268410) with nitrocellulose membrane filter of 0.22 μm pore size was utilized. From the absorbance spectra of MB recorded at different time intervals, the concentrations of MB in the reaction solution were estimated using a pre-calibrated concentration curve. The analyte concentration was determined using the most prominent absorption band of MB located at about 664.5 nm. The schematic diagram of the experimental setup is shows in Fig. 1.

3. RESULTS AND DISCUSSION

Fig. 2 shows the XRD patterns of the ZnO nanostructures prepared at different pH values (7.5, 8.0, 9.0 and 10) of the reaction mixture. All the samples revealed sharp, well-defined diffraction peaks, all matching with the wurtzite phase of ZnO (JCPDS Card No. 79-0207). The intensity of the main diffraction peaks like (101) and (002) varied from samples to sample due to the powder nature and different orientation of the nanostructures as reported by Jung et al.[30] However, the position of the diffraction peaks did not shift significantly with the variation of pH value.

Table 1. Position and FWHM of the main diffraction peaks, along with the lattice parameter values calculated from the XRD patterns of the ZnO nanostructures.

pH of the reaction mixture	Diffraction peak (101)		Diffraction peak (002)		Lattice parameters (Å)	
	2θ (deg.)	FWHM (deg.)	2θ (deg.)	FWHM (deg.)	*a*	*c*
pH 7.5	36.22	0.173	34.38	0.173	3.255	5.217
pH 8	36.22	0.176	34.40	0.199	3.256	5.214
pH 9	36.24	0.293	34.38	0.226	3.253	5.217
pH 10	36.24	0.299	34.42	0.244	3.254	5.211

From the diffraction peaks, the lattice constants of samples could be estimated as a = 3.25±0.01 Å and c = 5.21±0.01 Å (see Table 1). In general, the intensity of the (101) diffraction peak decreased and its full width at half maximum (FWHM) increased with the increase of NH_4OH concentration (increase of the pH value) in the reaction solution (see Table 1, Fig. 2b), indicating a possible decrease in crystallinity or an increase of defect content in the nanostructures.

Utilizing (101) diffraction peak, the average grain size (t) of the ZnO nanostructures was estimated using Debye Scherer equation:[31]

$$t = \frac{K\lambda}{B\cos\theta} \qquad (1),$$

where K is the shape factor (depends on the shape of the particles) considered to be 0.9, λ is the X-ray wavelength (λ=1.5406 Å), B is the FWHM of the (101) peak, and θ is the Bragg angle. Estimated average grain size values for the ZnO nanostructures grown at pH 7.5, 8, 9 and 10 were about 48, 47, 29 and 28 nm, respectively (Table 2). The decrease of grain size of the nanostructures at higher pH values of the reaction mixture is probably associated to the higher growth rate of the nanostructures.

To analyze the texture of the nanostructures, their N_2 adsorption-desorption isotherms were recorded at 77K. The porosity and specific surface area of the nanostructures were estimated from their isotherms using Brunauer-Emmett-Teller (BET) method.[32] Fig. 3 shows the typical N_2 adsorption-desorption isotherms of the as-grown ZnO nanostructures synthesized at different pH values of the reaction mixture. The N_2 adsorption-desorption behaviors of all the samples correspond to type III isotherm in Brunauer classification, with no limiting adsorption at high relative pressure in their hysteresis loops. According to the IUPAC classification, the observed hysteresis loops can be ascribed to type H3 of mesoporous material.[33] Estimated BET specific surface area of the nanostructures were

6.43, 3.83, 18.88, and 9.31 m^2 g^{-1} for the samples grown at pH 7.5, 8, 9, and 10, respectively (Table 2). As we can see, on increasing the pH of the reaction mixture, though the crystallite size (average grain size) of the samples decreased gradually, the BET specific surface area of the nanostructures does not follow such regular trend. However, the as-grown ZnO nanostructures prepared at pH 9 of the reaction mixture revealed highest specific surface area.

Typical SEM micrographs of the as-grown ZnO samples prepared at different pH values presented in Figure 4 shows the morphology of the nanostructures changes drastically with the variation of reaction pH. While the hexagonal nanodisks with an average diameter of 403 nm and average thickness of about 75 nm could be clearly observed (Fig. 4a) for the sample grown at pH 7.5, the sample prepared at pH 8 generated hexagonal dumbbell-shaped structures (Fig. 4b) of 300 - 600 nm diameters and up to 544 nm lengths. On increasing the pH of the reaction mixture to 9, rice-shaped ZnO nanostructures of 80-240 nm diameters and up to 547 nm length were produced (Fig. 4c). On increasing the pH of the reaction mixture further to 10, ZnO nanorods of 40 - 100 nm diameters and of 440 – 1400 nm lengths were produced (Fig. 4d). It should be noted that all these ZnO nanostructures were synthesized at room temperature, maintaining all the experimental conditions fixed, except solution pH, which was varied by the addition of ammonium hydroxide. Therefore, the evolution of diverse morphology of the nanostructures is believed to be the result of combined effects of the chelating agent EDTA and solution pH.

In aqueous solution, EDTA gets ionized completely and form metal ion complexes bonding with positively charged metal ions in the solution. Having four carboxyl groups and two neutral nitrogen atoms, EDTA acts as a hexadentate ligand to form metal ion complex as shown schematically in Figure 5. On the other hand, the formation of metal ion complex through EDTA ligand depends strongly on the pH of the medium.[34]

As has been discussed by several researchers,[35,36] prior to the addition of NH_4OH, the aqueous solution of $Zn(CH_3COO)_2 \bullet 2H_2O$ contains ionic and non-ionic species like Zn^{+2}, CH_3COO^-, $Zn(CH_3COO)(OH_2)_n$, $[Zn(OH)_4]^{2-}$, H_3O^+ and OH^-. On addition of EDTA (chelating agent), it makes zinc ion complex following the reaction:

$$Zn(CH_3COO)_2 \bullet 2H_2O + C_{10}H_{16}N_2O_8 + H_2O \longrightarrow Zn(C_{10}H_{16}N_2O_8) + 2CH_3COO^- + 3H_2O \quad (2).$$

On the addition of NH_4OH to this mixture solution, zinc hydroxide [$Zn(OH)_2$] is formed, which under ultrasonic irradiation dissociates to form solid ZnO molecules following the reactions:

$$NH_4OH \longrightarrow NH_4^+(aq) + OH^-(aq) \quad (3)$$

$$Zn(C_{10}H_{16}N_2O_8) + 2\,OH^- \longrightarrow Zn(OH)_2 + C_{10}H_{16}N_2O_8 \quad (4)$$

and

$$Zn(OH)_2 \xrightarrow{)))} ZnO(s) + H_2O \quad (5),$$

where the symbol))) denotes ultrasonic irradiation. When the concentration of NH_4OH in the reaction mixture is very high (at higher pH values of the reaction mixture), the earlier formed $Zn(OH)_2$ reacts with the excess hydroxyl ions to form stable $[Zn(OH)_4]^{2-}$ complex, which acts as the growth unit of ZnO nanostructures. Therefore, the sonochemical growth of the ZnO nanostructures at very high pH values of the reaction mixture follows the reactions:

$$Zn(OH)_2 + 2\,OH^- \longrightarrow [Zn(OH)_4]^{2-} \quad (6)$$

$$[Zn(OH)_4]^{2-} \xrightarrow{)))} ZnO + H_2O + 2OH^- \quad (7).$$

Table 2. Morphology, average grain size and specific surface area of the as-grown and annealed ZnO nanostructures grown at different pH values of the reaction mixture.

pH of the reaction mixture	Observed morphology	as-grown		annealed	
		Average grain size (nm)	BET specific surface area (m^2/g)	Average grain size (nm)	BET specific surface area (m^2/g)
7.5	Hexagonal disks	48	6.43	43	2.82
8	Dumbbell-shaped	47	3.83	39	2.58
9	Rice-like	29	18.88	25	2.20
10	Rods	28	9.31	29	5.16

Fig. 6 shows a schematic illustration of the formation process of ZnO nanostructures of hexagonal disk, dumbbell-shaped bipods, rice-shaped, and rod-like morphologies. At pH 7.5, the hexagonal nanodisks were formed due to the growth of ZnO along the 6-fold symmetric directions perpendicular to [001]. When the pH of the reaction mixture was

increase to 8, the dumbbell-shaped bipod structures were grown preferentially along the [001] direction. At pH 9, the growth rate of the small ZnO nuclei along the [001] direction increases and decreases along its perpendicular directions, forming rice-like morphologies. Finally, on increasing the pH of the reaction mixture to 10, the nanostructures grow solely along [001] direction, forming nanorod structures of uniform diameters. The growth behavior of the nanostructures along their preferential crystallographic directions as discussed above are also reflected in their XRD patterns presented in Fig. 2.

The UV-Vis diffuse reflectance spectra of the ZnO nanostructures grown at different pH values are presented in Figure 7. All the samples revealed a sharp absorption edge at about 375 nm, characteristic of crystalline ZnO. From the figure, we can see that at about 420 nm the reflectance drops steeply with the decrease of wavelength and attains a plateau at around 375 nm. While the position of absorption edge did not change drastically, it shifts marginally towards lower wavelength side (higher energy) with the increase of solution pH. The estimated direct band gap energy were 3.24, 3.25, 3.30, and 3.26 eV for the samples prepared at pH 7.5, 8, 9, and 10, respectively. While the band gap energy values of all the samples are lower than the known band gap energy of pure ZnO (3.37 eV), it is closest only for the sample prepared at pH 9. Although, such lower band gap energy values have been reported for metal ion doped ZnO samples by several researchers,[28,37,38] presence of structural and electronic defects such as interstitials and vacancies created during synthesis process has also seen to reduce the band gap energy of undoped ZnO.[39] The contributions of such defect sites on the PL emission behavior and catalytic activity of the nanostructures have been discussed later.

3.1. Photocatalytic activity

The photocatalytic behavior of the ZnO nanostructures was analyzed by monitoring their MB decomposition rates under ultraviolet (365 nm, 10 W) radiation. All the samples were tested under similar experimental conditions utilizing a jacketed mini-reactor. About 100 mg of ZnO nanostructures were dispersed in 100 mL of aqueous MB (10 ppm) solution. Prior to UV irradiation, the suspensions were magnetically stirred in the dark for about 60

minutes to establish the adsorption/desorption equilibrium of MB on catalyst. The residual concentration of MB was monitored by measuring the absorbance of the samples using a UV-Vis-NIR spectrophotometer in liquid cuvette configuration with DI water as reference. The progress of the reaction was followed by monitoring the intensity of the MB absorption band at 664.5 nm. The percentage of degradation was calculated using the Bear Lambert relation:

$$Degradation\ (\%) = \frac{C_0 - C}{C_0} \times 100 \quad (8)$$

where C_0 is the initial dye concentration and C is the dye concentration at time t from the start of photocatalytic reaction.

Figure 8a shows the time-dependent absorption spectra of MB solution (10 ppm) under UV irradiation in contact with ZnO nanostructures prepared at pH 9. The intense absorption band appeared at about 612 nm corresponds to the dimer of MB [(MB)2], and the most intense absorption peak appeared around 664.5 nm corresponds to the monomer of MB.[40] For the quantitative analysis of MB photo-degradation process, the later absorption band was monitored. As we can see, the intensity of the 664.5 nm absorption band of MB steadily decreases with UV irradiation time. After about 30 minutes of UV irradiation, the intensity of the absorption band decreased to about 22.9 %, and almost a complete degradation of MB could be achieved in about 240 minutes.

For comparison, the adsorption and photo-degradation rates of MB for all the ZnO nanostructures are presented in Figure 8b. The MB photo-degradation rate of all the ZnO samples decreased gradually with time. The photocatalytic performance of ZnO nanostructures grown at pH 9 is much superior to the nanostructures grown at other pH values. The higher photocatalytic activity of the ZnO nanostructures prepared at pH 9 could be due to their higher specific surface area (18.88 m^2/g) than the other ZnO nanostructures (Table 2). The nanostructures of higher surface area make a larger contact area with the target material, absorbing higher amount of MB molecules. Mekasuwandumrong et al.[41] have also observed a higher photocatalytic activity of ZnO nanoparticles of smaller sizes in the degradation of MB, and attributed to their higher BET surface area. On the other hand, for Ta-doped ZnO nanoparticles, Kong et al.[10] observed highest photo-degradation efficiency for the sample annealed at 700 °C. The high photocatalytic activity of the

annealed ZnO:Ta was attributed to a competitive trade-off among the preferable crystallinity, optimal quantity of hydroxyl groups on the catalyst surface, and larger specific surface area. As has been mentioned above, a complete MB degradation was observed after 240 minutes of UV irradiation for the nanostructures grown at pH 9. On the other hand, for the same duration of UV exposure, about 91.6, 73.4, and 64.7 % MB degradation occurred for the ZnO nanostructures grown at pH 7.5, 8, and 10, respectively. We believe the highest photocatalytic activity of our ZnO nanostructures grown at pH 9 is due to their higher specific surface area and higher defect content of electron trapping character than the other nanostructures.

To estimate the defect contents in the nanostructures qualitatively, their room temperature photoluminescence spectra were recorded (Fig. 9). All the samples revealed a broad defect emission in the visible range (470-750 nm), apart from their typical near band edge (NBE) emission associated to excitonic transition at about 376 nm (3.3 eV).[42,43] While the position of the NBE emission for the samples prepared at pH 7.5 and 8 remained at about 386 nm, its position shifted to 393 and 390 nm for the samples grown at pH 9 and 10, respectively. The red-shift of the NBE band for the later samples could be associated to the competitive evolution of the free excitons (FXs) and neutral donor-bound excitons, or their phonon replicas associated to defect incorporation, as has been discussed in our earlier works.[42,44] As we can see from the NBE normalized PL spectra of the samples presented in Figure 9, although the position of the defect-induced visible emission band (~ 575 nm) does not change from sample to sample, its intensity varied drastically with the variation of reaction pH. From the I_{Vis}/I_{UV} intensity ratio plotted against solution pH presented as inset of Figure 9, it is very clear that the sample prepared as pH 9 contains highest defect concentration. The variation of defect concentration in the samples is probably associated to their different growth rates and exposed crystalline surfaces of different orientations (with different atomic arrangements). Therefore, the highest photocatalytic activity of the sample grown at pH 9 must be associated to its higher specific surface area (18.88 m^2g^{-1}) and higher content of electron trapping defects.

The broad emission band in the visible region could be deconvoluted into three Gaussian shaped components (Fig. 9 b) peaked around 568 nm (2.18 eV), 706 nm (1.75 eV), and 770 nm (1.61 eV). While the component band close to 2.18 eV, frequently assigned as yellow

emission, has been associated with interstitial oxygen (O_i) in ZnO,[45] the component around 1.75 eV has been assigned as the red emission, attributed to oxygen vacancies (V_O).[46] On the other hand, the component band around 770 nm (1.61 eV) has been rarely observed for pure ZnO and assigned as the red or red-NIR emission associated to interstitial oxygen[47] or the combination of oxygen interstitial and oxygen vacancies.[46]

As the Figure 9 shows, the intensity of the defect induced visible emission increases with the increase of reaction pH until 9, and then decreases. While the intensity of the O_i induced emission peaked around 568 nm is highest for the sample prepared at pH 9, the intensity of the O_i induced red emission around 770 nm is highest for the sample grown at pH 7.5. On the other hand, the intensity of the V_O related emission around 706 nm is highest for the sample grown at pH 9. In fact, the nature and concentration of surface defects (interstitial oxygen and oxygen vacancies) in the nanostructures are quite different for the samples prepared at different pH values. As the photocatalytic activity of nanostructured catalysts depends strongly on the concentration of surface defects (discussed later), samples prepared at different reaction pH are expected to have very different catalytic activity for the degradation of organic dyes.

3.2. Mechanism of photocatalytic degradation

The mechanism of MB photo-degradation over ZnO has already been reported by several researchers.[48-50] When the photocatalyst ZnO is illuminated with photons of energy equal to or greater than its band-gap energy,[51] valence band electrons will be excited to the conduction band producing electron-hole pairs, which diffuse to or near the catalyst surface. This state is referred as the semiconductor's photo-excitation state. The production of photoinduced electron-hole can be expressed by the relation:

$$ZnO + hv \rightarrow ZnO + h_{vb}^{+} + e_{cb}^{-} \quad (9).$$

The photo-generated holes move to the surface, and react with surface OH^- groups and H_2O to produce HO• radicals, which get absorbed on the ZnO surface (eqs 10 and 11). These surface absorbed hydroxyl radicals (HO•), which are known to be strong oxidizing

species, react with the MB adsorbed at the surface of the catalyst, mineralizing the compound partially or completely (eq 12) following the reactions:

$$h_{vb}^{+} + H_2O \rightarrow OH^{\bullet} + H^{+} \quad (10)$$

$$h_{vb}^{+} + OH^{-} \rightarrow OH^{\bullet} \quad (11)$$

$$OH^{\bullet} + MB \rightarrow degradation\ of\ MB \quad (12).$$

On the other hand, O_2 plays an important role in these reactions. The electrons in the conduction band can reduce O_2 to produce superoxide radicals ($O_2^{\bullet}$) (eq 13). Subsequently these $O_2^{\bullet}$ radicals react with hydrogen ions generated through water splitting to form hydroperoxyl $HO_2^{\bullet}$ (eq 14) radical and other reactive oxygen species such as H_2O_2 and $OH^{\bullet}$ (eqs 15 and 16).

$$O_2 + e_{cb}^{-} \rightarrow O_2^{\bullet} \quad (13)$$

$$O_2^{\bullet} + H^{+} \rightarrow HO_2^{\bullet} \quad (14)$$

$$2OH^{\bullet} \rightarrow H_2O_2 \quad (15)$$

$$H_2O_2 + e_{cb}^{-} \rightarrow OH^{\bullet} + OH^{-} \quad (16)$$

The HO• radicals are the most important oxidants formed in a photocatalytic process responsible for the degradation of organic compounds (eq 12).

As has been explained by Zheng et al.,[52] the defects like interstitial oxygen (O_i) generate shallow levels near the valence band (VB), acting as traps for photogenerated holes. On the other hand, defects like oxygen vacancies (V_O**)** work as electron acceptors, which can trap the photogenerated electrons temporarily, reducing the surface recombination of electrons and holes.

3.3. Kinetic study

The steady-state photocatalytic rate of a heterogeneous system can be expressed through Langmuir-Hinshelwood relation. The relation describes the pseudo first-order kinetics,[53,54] where the initial concentration of the solution affects the photocatalytic degradation rate of most of the organic compounds. The photocatalytic degradation of MB by ZnO nanostructures grown at different pH values of the reaction solution obeyed the pseudo-

first-order kinetics. At low initial dye concentration, the simplest representation for the rates of photodegradation of MB can be given by:

$$\ln C = -kt + \ln C_0 \quad (17).$$

This equation can be used to demonstrate linearity of data, if the integration of (eq 22) is given by:

$$\ln (C_0/C) = kt \quad (18)$$

where k is the constant of the pseudo-first-order rate. A plot of ln (C_0/C) versus the UV irradiation time for the MB photo-degradation by the as-grown ZnO nanostructures is shown in Figure 10. Linear relations between ln (C_0/C) and the time of UV-irradiation for all the as-grwon ZnO nanostructures indicate the photo-degradation process follows first-order kinetics. The values of the pseudo-first-order rate constant k could be obtained directly from the linear regression curves (linear fits) shown in Fig. 10. The estimated values of k, $t_{1/2}$ (half-life) and corresponding correlation coefficients (R^2) for the as-grown ZnO nanostructures are listed in Table 3. As a higher value of k is indicative of outstanding photocatalytic performance of a catalyst, the 1.59×10^{-2} min^{-1} and 43.58 min values for k and $t_{1/2}$, respectively, for the ZnO nanostructures grown at pH 9 indicate their excellent photocatalytic activity.

Table 3. Pseudo-first order rate constant (k), the half-life ($t_{1/2}$), and R^2 of MB degradation by the as-grown and air-annealed ZnO nanostructures.

pH of the reaction mixture	as-grown			Annealed		
	k (min^{-1})	$t_{1/2}$ (min)	R^2	K (min^{-1})	$t_{1/2}$ (min)	R^2
7.5	8.30E-03	83.5	0.992	2.09E-02	33.0	1
8	4.40E-03	157.5	0.999	1.71E-02	40.5	0.98
9	1.59E-02	44.0	0.974	1.26E-02	55.0	0.95
10	3.30E-03	210	0.983	1.53E-02	45.0	0.99

3.4. Effect of carbon contamination

As the dye-degradation at semiconductor surface depends on the charge transfer process at semiconductor interface, presence of any surface imperfection/impurity can alter the photocatalytic performance of a heterogeneous catalyst. In fact, the presence of surface contamination either of organic or inorganic nature can influence the photocatalytic performance of a catalyst.[55,56] Most of the organic compounds in contact with semiconductor surface act as hole scavengers, affecting the charge recombination process[54] and hence the its photocatalytic performance.

As all the ZnO nanostructures of present study were synthesized by the hydrolyzing zinc acetate through ultrasonication, and ethanol was used to wash them, carbon contamination in the nanostructures is expected. To remove carbon from the surface of the nanostructures, we annealed them at 525^0C for 3 h in air, and measured their N_2 adsorption-desorption isotherms and photocatalytic performance for MB degradation.

The N_2 adsorption-desorption isotherms of air-annealed ZnO nanostructures revealed a shrinkage in specific surface area for all the samples. While the morphology of the nanostructures (not shown) did not change after air annealing, the BET estimated specific surface areas were 2.82, 2.58, 2.20, and 5.16 m^2/g for the nanostructures grown at pH 7.5, 8, 9, and 10, respectively (Table 2). After air annealing, the photocatalytic performance of all the samples improved noticeably (Fig. 11a). While a complete MB degradation was obtained for the sample prepared at pH 7.5 in 180 minutes of UV irradiation, for all other samples, higher than 80% degradation could be achieved within 190 minutes. It should be noted that the order of MB degradation efficiency of the nanostructures grown at different pH values changed drastically after air annealing, and the most efficient sample does not have the highest specific surface area. This drastic change in photocatalytic performance of the air-annealed samples can be associated to the elimination of carbon contaminant from their surface and the change of their specific surface area. As can be noticed, while after air annealing, the specific surface area of the samples grown at pH 7.5 and 9 become similar, the earlier sample shows highest catalytic efficiency and the later lowest. As the average grain size of the samples did not change significantly after air annealing (Table 2), the change in photocatalytic performance of the nanostructures cannot be associated to their

grain size or a change in grain boundary area. Though since long the photocatalytic performance of nanostructured ZnO has been associated to their particle size, specific surface area, defect content, surface contamination, and even to their morphology, present study indicates the morphology of the nanostructures has no direct contribution to their photocatalytic behaviors. While after air annealing the content of carbon in all the samples reduced significantly, along with their specific surface area, their stoichiometry (Table 4) also varied. Although the specific surface area for the sample prepared at pH 9 reduced drastically, the reduction is not so drastic for the other samples. On the other hand, while after air annealing the composition of the sample prepared at pH 9 did not change significantly, the stoichiometry of all other samples suffered a drastic change, reducing Zn/O ratio significantly. The reduction of Zn/O ratio is highest for the sample prepared at pH 7.5. Such a variation of sample stoichiometry and its effect on defect distribution in the samples have been reflected in their PL spectra presented in Figure 9.

As the specific surface area and defect content in metal oxide nanostructures influence directly to their ability for dye capture and trapping ability of photo-generated charge carriers (electrons and holes), they are the main factors, apart from carbon contaminant, which define their photocatalytic performances. While the highest photocatalytic efficiency of our as-gown sample prepared at pH 9 is probably due to their high specific surface area and higher defect content of O_i nature, the improved photocatalytic performance of the air-annealed sample prepared at pH 7.5 can be associated to its off-stoichiometric composition with higher defect contents of O_i and V_o natures. It should be remembered that after air annealing, the photocatalytic performance of all the samples prepared in the present study improved. Therefore, while preparing ZnO nanostructures for their photocatalytic applications, along with contaminants, we must take care of their specific surface area and defects contents, which affect even more profoundly.

Table 4. EDS estimated Zn/O atomic ratio and carbon content in the ZnO nanostructures grown at different pH values.

pH of the reaction mixture	as-grown		annealed	
	C (at. %)	Zn/O (at. ratio)	C (at. %)	Zn/O (at. ratio)
7.5	14.8	0.81	13.76	0.60

8	21.18	0.83	15.51	0.66
9	17.07	0.65	14.57	0.63
10	29.74	0.86	24.74	0.69

To study the reusability of the air-annealed ZnO nanostructures, we performed repeated photocatalytic tests of the air-annealed ZnO sample synthesized at pH 7.5 (Fig. 12). As can be seen, even after 6 cycles of reuse, the photocatalytic performance of the nanostructures did not change drastically. As the size of the nanostructures were relatively big, after each cycle, they could be separated from the reaction mixture easily by decantation.

Conclusions

ZnO nanostructures of hexagonal disk, dumbbell-shaped bipod, rice-shaped and rod shaped morphologies could be successfully fabricated by ultrasound-assisted hydrolysis of zinc acetate in water using EDTA as chelating agent. Both the morphology and defect content in the nanostructures depend strongly on the pH of the reaction mixture. The morphology of the nanostructures has no direct effect on their photocatalytic performance for MB degradation under UV illumination. However, the specific surface area, the nature and concentration of electronic defects, as well as surface contaminants have strong effects to their photocatalytic performance. While the rice-shaped as-grown ZnO nanostructures grown at pH 9, with highest specific surface area and highest defect content show highest photocatalytic activity for MB degradation; after air annealing, the hexagonal disk shaped ZnO nanostructures become most active photocatalyst. It has been demonstrated that for photocatalytic applications of ZnO nanostructures, they should be of higher specific surface area, free from carbon like contaminants and contain high concentration of electronic defects like interstitial oxygen and/or oxygen vacancies.

Acknowledgements

The authors acknowledge the National Nanoscopy Laboratory of CINVESTAV, Mexico for recording SEM images of the nanostructures. The work was financially supported by CONACyT and VIEP-BUAP, Mexico, through the project grants # CB-2010/151767 and VIEP/EXC/2014, respectively.

Author information

Corresponding author

* E-mail: upal@ifuap.buap.mx

Fax: +52-222-2295611

Notes and References

[a]Centro de Investigación en Dispositivos Semiconductores, ICUAP, Benemérita Universidad Autónoma de Puebla, Puebla, Pue. 72570, Mexico. [b]Instituto de Física, Benemérita Universidad Autónoma de Puebla, Apdo. Postal J-48, Puebla, Pue. 72570, Mexico.

1 A. O. Ibhadon and P. Fitzpatrick, *Catalysts,* 2013, **3**, 189-218.

2 J. Matos, J. Laine and J. M. Herrmann, *J. Catal,*. 2001, **200**, 10–20.

3 A. Fujishima, T. N. Rao and D. A. Tryk, *J. Photochemistry and Photobiology C:Photochem. Rev*., **2000**, 1, 1–21.

4 B. Dindar and S. Icli, *J. Photochemistry and Photobiology A:Chemistry,* 2001, **140**, 263–268.

5 N. Daneshvar, D. Salari and A. R. Khataee, *J. Photochemistry and Photobiology A: Chemistry,* 2004, **162**, 317–322.

6 P. V. Kamat, *J. Phys. Chem. Lett*., 2010, **1**, 520–527.

7 E. Wilson, *Chem. Eng. News,* 1996, **74**, 29-33.

8 M. I. Cabrera, O. M. Alfano and A. E. Cassano, *J. Phys. Chem.,* 1996, **100**, 20043-20050.

9 G. Voicu, O. Oprea, B. S. Vasile and E. Andronescu, *Digest J. Nanomaterials and Biostructures,* 2013, **8**, 667–675.

10 J. Z. Kong, A. D. Li, X. Y. Li, H. F. Zhai, W. Q. Zhang, Y. P. Gong, H. Li and D. Wu, *J. Solid State Chem.,* 2010, **183**, 1359–1364.

11 J. Kaur, S. Bansal and S. Singhal, *Physica B,* 2013, **416**, 33–38.

12 R. Kumar, G. Kumar and A. Umar, *Mater. Lett*., 2013, **97**, 100–103.

13 M. L. Curri, R. Comparelli, P. D. Cozzoli, G. Mascolo and A. Agostiano, *Mater. Sci. Eng. C,* 2003, **23**, 285–289.

14 H. R. Ebrahimi and M. Modrek, *J. Chem*., 2013, **2013**, 1-5.

15 M. A. Kanjwal, N. A. M. Barakat, F. A. Sheikh, W-l. Baek, M. S. Khil and H. Y. Kim, *Fibers and Polymers,* 2010, **11**, 700–709.

16 N-A. M. Barakat, M. A. Abdelkareem, M. El-Newehy and H. Y. Kim, *Nanoscale Res. Lett*., 2013, **8**, 402-1 - 402-6.

17 M. C. Yeber, J. Rodríguez, J. Freer, J. Baeza, N. Durán and H. D. Mansilla, C*hemosphere,* 1999, **39**, 1679–1688.

18 A. Akyol, H. C. Yatmaz and M. Bayramoglu, *Appl. Catal. B,* 2004, **54**, 19-24.

19 J. C. Lee, S. Park, H-J. Park, J-H. Lee, H-S. Kim and Y-J. Chung, *J. Electroceram*., 2009, **22**, 110–113.

20 C. Wang, X. Wang, B.Q. Xu, J. Zhao, B. Mai, P. Peng, G. Sheng and J. Fu, *J. Photochem. Photobiol. A: Chem*., 2004, **168**, 47-52.

21 S. Chakrabarti and B. K. Dutta, *J. Hazard. Mater. B,* 2004, **112**, 269-278.

22 S. Khezrianjoo and H. D. Revanasiddappa, *J. Catalysts,* 2013, **2013**, 582058-1 - 582058-6.

23 H. D. Jang, S-K. Kim and S-J. Kim, *J. Nanopart. Res*., 2001, **3**, 141–147.

24 V. S. Smitha, P. Francois, U. N. S. Hareesh and K. G. Warrier, *J. Mater. Chem. A,* 2013, **1**, 12178-12187.

25 C. B. Almquist, P. Biswas, *J. Catalysis,* 2002, **212,** 145–156.

26 J. Yu and X.Yu, *Environ. Sci. Technol*., 2008, **42**, 4902–4907.

27 M. J. Height, S. E. Pratsinis, O. Mekasuwandumrong and P. Praserthdam, *Applied Catalysis B: Environmental,* 2006, **63**, 305–312.

28 R. Ullah and J. Dutta, *J. Hazard. Mater*., 2008, **156**, 194–200.

29 R. Wang, J. H. Xin, Y. Yang, H. Liu, L. Xu and J. Hu, *Appl. Surf. Sci*., 2004, **227**, 312–317.

30 S. H. Jung, E. Oh, K. H. Lee, Y. Yang, C. G. Park, W. Park and S. H. Jeong, *Cryst. Growth & Design,* 2008, **8**, 265-269.

31 B. D. Cullity, *Elements of X-Ray Diffraction*, Ed. Addison-Wesley Publishing Company, Inc., 1956; pp 93-98.

32 S. Brunauer, P. H. Emmett and E. Teller, *J. Am. Chem. Soc*., 1938, **60**, 309-319.

33 A-H. Lu, D. Zhao and Y. Wan, *Nanocasting,* Ed. RSC Publishing. RSC Nanosci. Nanotechnol. United Kingdom, 2010, pp 34-37.

34 D. C. Harris, *Quantitative Chemical Analysis*, Ed. Reverte, 2nd Edition, 2006.

35 Y. Wang, Y. Li, Z. Zhou, X. Zu and Y. Deng, *J. Nanopart. Res*., 2011, **13**, 5193–5202.

36 F. A. Cotton and G. Wilkinson, *Advanced inorganic chemistry. A comprehensive text*, Ed. New York, Wiley-Interscience, 5th Edition, 1980.

37 X. Qiu, L. Li, J. Zheng, J. Liu, X. Sun and G. Li, *J. Phys. Chem. C.,* 2008, **112,** 12242.

38 J.T. Luo, Y. C.Yang, X. Y. Zhu, G. Chen, F. Zeng and F. Pan, *Phys. Rev. B.,* 2010, **82,** 014116.

39 S. Baruah, M. A. Mahmood, M.T.Z. Myint, T. Bora and J. Dutta, *Beilstein J. Nanotechnol*., 2010, **1**, 14-20.

40 G. Voicu, O. Oprea, B. S. Vasile and E. Andronescu, *Digest J. Nanomater. Biostructures,* 2013, **8**, 667 – 675.

41 O. Mekasuwandumrong, P. Pawinrat, P. Praserthdam and J. Panpranot, *Chem. Eng. J*., 2010, **164**, 77–84.

42 E. M. Alejandro and P. Umapada, *Appl. Phys. Lett*., 2008, **93**, 193120-1 - 193120-3.

43 C. Ton-That, M. Foley and M. R. Phillips, *Nanotechnol*., 2008, **19**, 415606-1 - 415606-5.

44 S. Z. Raul, B. F. Marcelino and P. Umapada, *J. Appl. Phys*., 2011, **109**, 014308-1 - 014308-6.

45 Wu, X.L.; Siu, G.G.; Fu, C.L.; Ong, H.C. *Appl. Phys. Lett.* 2001, **78**, 2285–2287.

46 N. H. Alvi, K. U. Hasan, O. Nur and M. Willander, *Nanoscale Res. Lett.*, 2011, **6**, 130.

47 A. B. Djurisic and Y. H. Leung, *Small*, 2006, **2**, 944-961.

48 L. Zhang, L. Du, X. Cai, X. Yu, D. Zhang, L. Liang, P. Yang, X. Xing, W. Mai, S.Tan, Y. Gu and J. Song, *Physica E,* 2013, **47**, 279–284.

49 S. Kant and A. Kumar, *Adv. Mater. Lett*., 2012, **3**, 350-354.

50 M. M. Rashad, A. A. Ismail, I. Osama, I. A. Ibrahim and A.-H. T. Kandil, *Arabian J. Chem*., 2014, **7**, 71-77.

51 J.-M. Herrmann, *Appl. Photocatal.,* 2005, **34**, 49-65.

52 Y. H. Zheng, C. Q. Chen, Y. Y. Zhan, X. Y. Lin, Q. Zheng, K. M. Wei, J. F. Zhu and Y. J. Zhu, *Inorg. Chem*., 2007, **46**, 6675-6682.

53 H.K. Yadav, K. Sreenivas, R.S. Katiyar and V.Gupta, *J. Phys. D:Appl. Phys.,* 2007, **40**, 6005–6009.

54 J. Serrano, A.H. Romero, F. J. Manjon, R. Lauck, M. Cardona and A. Rubio, *Phys. Rev. B,* 2004, **69**, 094306-1 - 094306-14.

55 C. Hariharan, *Appl. Catal. A:General,* 2006, **304**, 55–61.

56 P. V. Kamat and B. Patrick, *J. Phys. Chem.,* 1992, **96**, 6829-6834.

Table and Figure captions:

Table 1. Position and FWHM of the main diffraction peaks, along with the lattice parameter values calculated from the XRD patterns of the ZnO nanostructures.

Table 2. Morphology, average grain size and specific surface area of the as-grown and annealed ZnO nanostructures grown at different pH values of the reaction mixture.

Table 3. Pseudo-first order rate constant (k), the half-life ($t_{1/2}$), and R^2 of MB degradation by the as-grown and air-annealed ZnO nanostructures.

Table 4. EDS estimated Zn/O atomic ratio and carbon content in the ZnO nanostructures grown at different pH values.

Fig. 1 Schematic diagram of the experimental set-up used for photocatalytic tests.

Fig. 2 (a) Full-scale XRD patterns of the ZnO nanostructures prepared at different pH values, and (b) the positions of (002) and (101) peaks in amplified scale. The vertical red lines adjusted to the positions of (002) and (101) peaks of the sample prepared at pH 7.5 to show the peak shifts for other samples.

Fig. 3 Typical N_2 adsorption-desorption isotherms for ZnO nanostructures grown at different pH values of the reaction mixture.

Fig. 4 Typical SEM micrographs of the ZnO nanostructures grown at a) pH 7.5, b) pH 8, c) pH 9, and d) pH 10 of the reaction mixture.

Fig. 5 a) Ion structure, b) skeletal formula, and c) metal ion complex of EDTA. M denotes a metal ion.

Fig. 6 Schematic illustration of the formation process of ZnO nanostructures with hexagonal disks, dumbbell-shaped bipods, rice-like and rod-like morphologies.

Fig. 7 DRS spectra of the as-grown ZnO nanostructures prepared at different pH values of the reaction mixture.

Fig. 8 a) MB absorbance spectra used to determine the photocatalytic activity of as-grown ZnO nanostructures prepared at pH 9, and b) photo-degradation rate of MB over as-grown ZnO nanostructures prepared at different pH values of the reaction mixture. The MB degradation behavior under UV illumination has also been included to show that there is no photo-degradation of MB in absence of catalyst.

Fig. 9 (a) (a) Room temperature PL spectra of the as-grown ZnO nanostructures prepared at different pH values of the reaction mixture. The inset shows the variation of I_{Vis}/I_{UV} intensity ratio with solution pH. (b) Gaussian deconvolution of the visible PL band for the ZnO nanostructures.

Fig. 10 Kinetic fits ($\ln(C_0/C)$ vs. time) for the photocatalytic degradation of MB by as-grown ZnO nanostructures prepared at different pH values.

Fig. 11 a) MB photo-degradation by the air-annealed (at 525°C for 3 h in air) ZnO nanostructures, and b) kinetic fits ($\ln(C_0/C)$ vs. time) for the photocatalytic degradation of MB.

Fig. 12 Reusability test for the air-annealed ZnO nanostructures grown at pH 7.5. The estimated degradation % correspond to 180 min of degradation time.

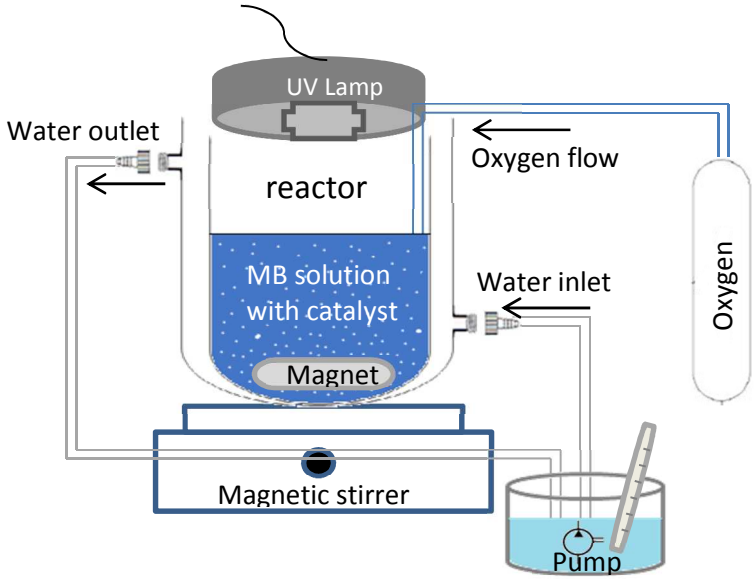

Fig. 1 Schematic diagram of the experimental set-up used for photocatalytic tests.

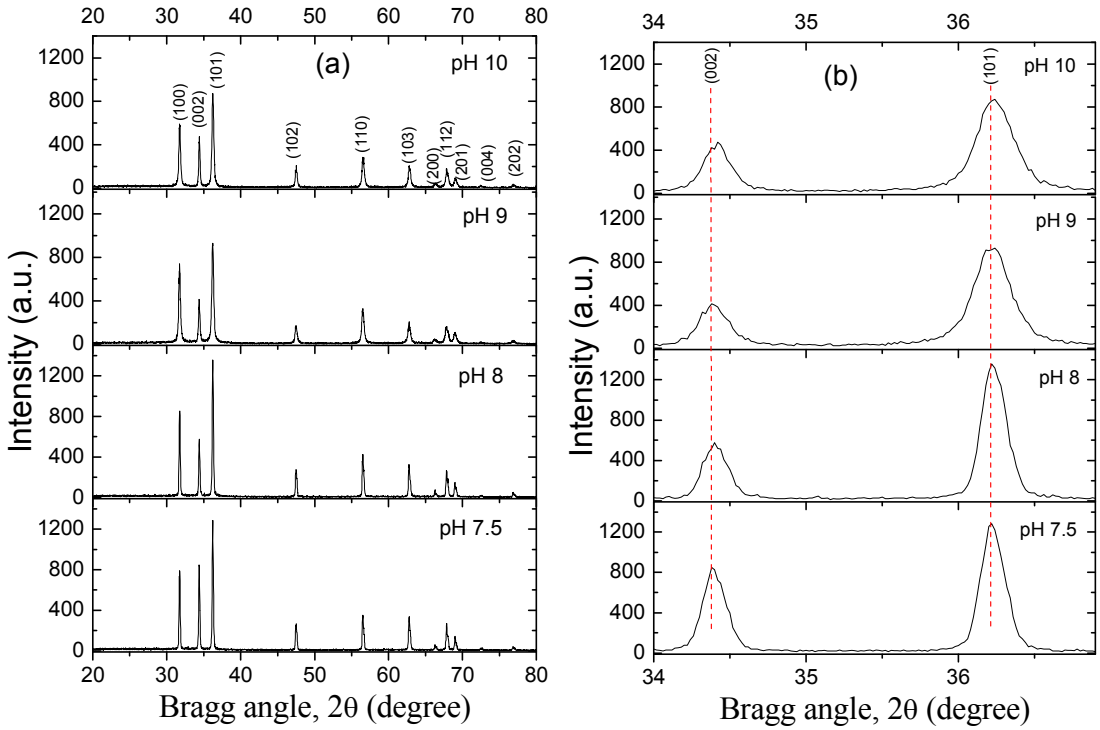

Fig. 2 Full-scale XRD patterns of the ZnO nanostructures prepared at different pH values, and (b) the positions of (002) and (101) peaks in amplified scale. The vertical red lines adjusted to the positions of (002) and (101) peaks of the sample prepared at pH 7.5 to show the peak shifts for other samples.

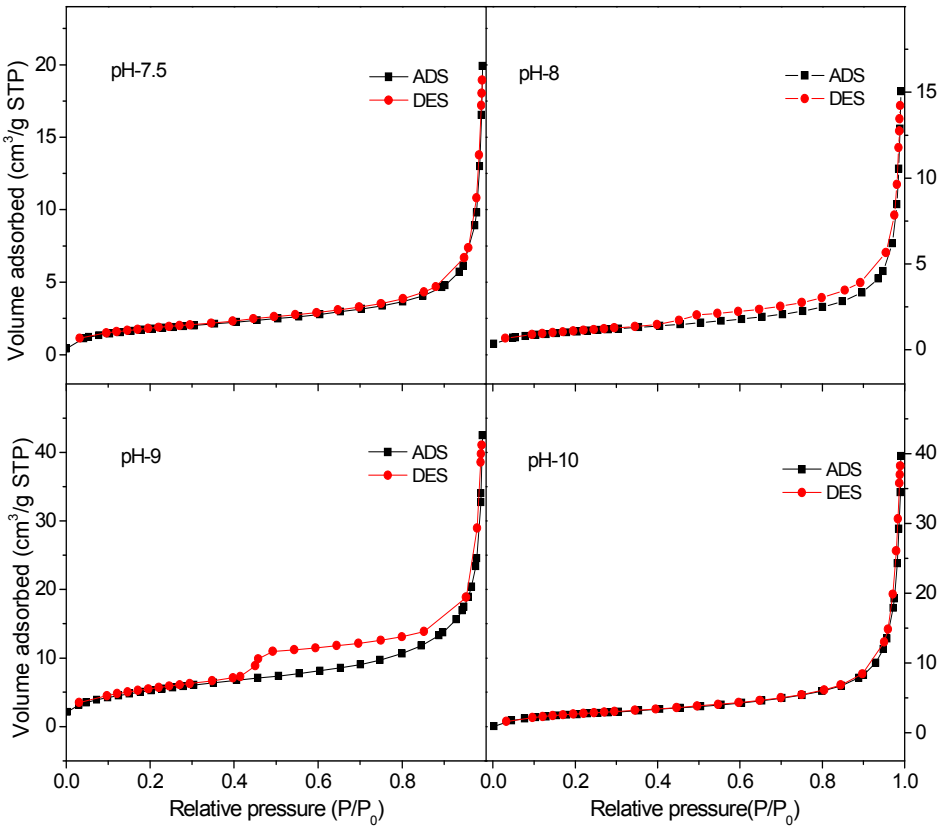

Fig. 3 Typical N_2 adsorption-desorption isotherms for ZnO nanostructures grown at different pH values of reaction mixture.

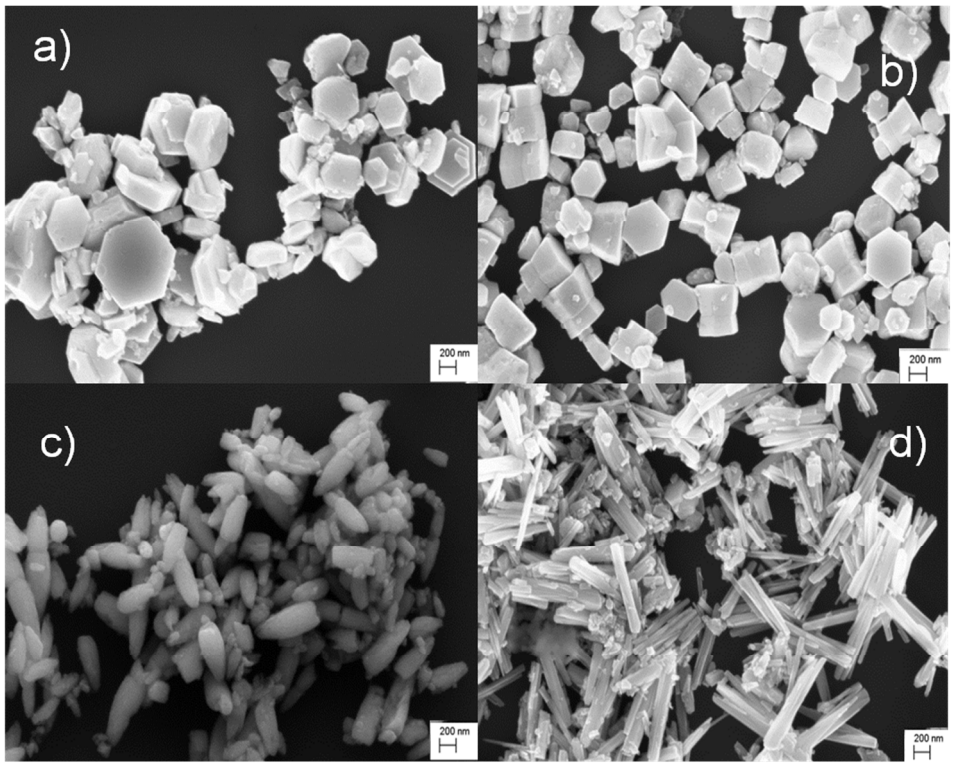

Fig. 4 Typical SEM micrographs of the ZnO nanostructures grown at a) pH 7.5, b) pH 8, c) pH 9, and d) pH 10 of the reaction mixture.

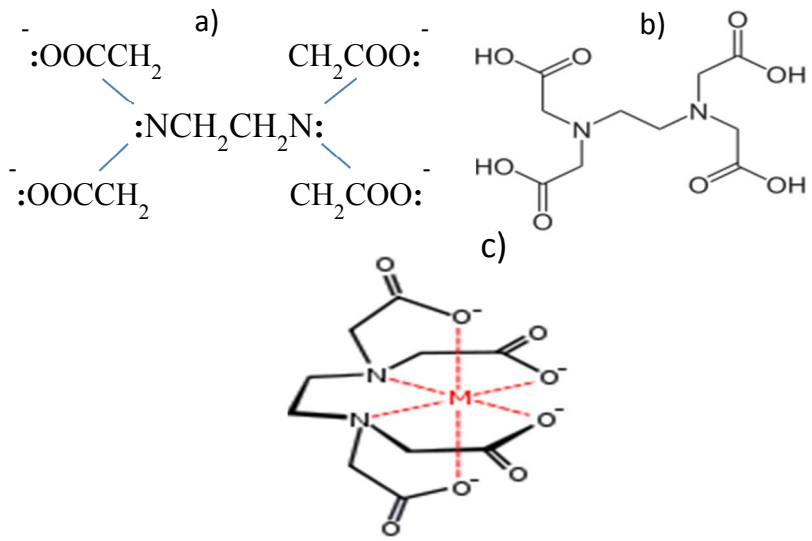

Fig. 5 a) Structure of the ion, b) skeletal formula, and c) metal ion-EDTA complex. M denotes the metal ion.

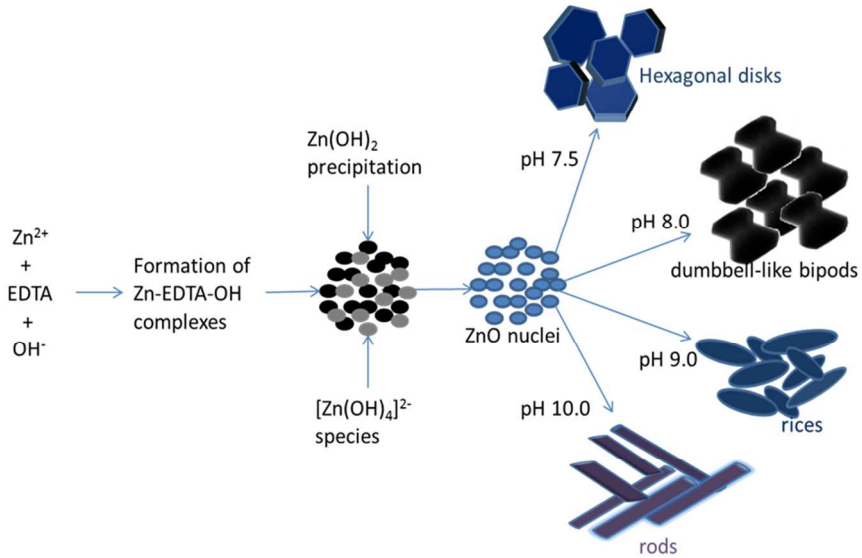

Fig. 6 Schematic illustration of the formation process of ZnO nanostructures with hexagonal disks, dumbbell-shaped bipods, rice-like and rods morphologies.

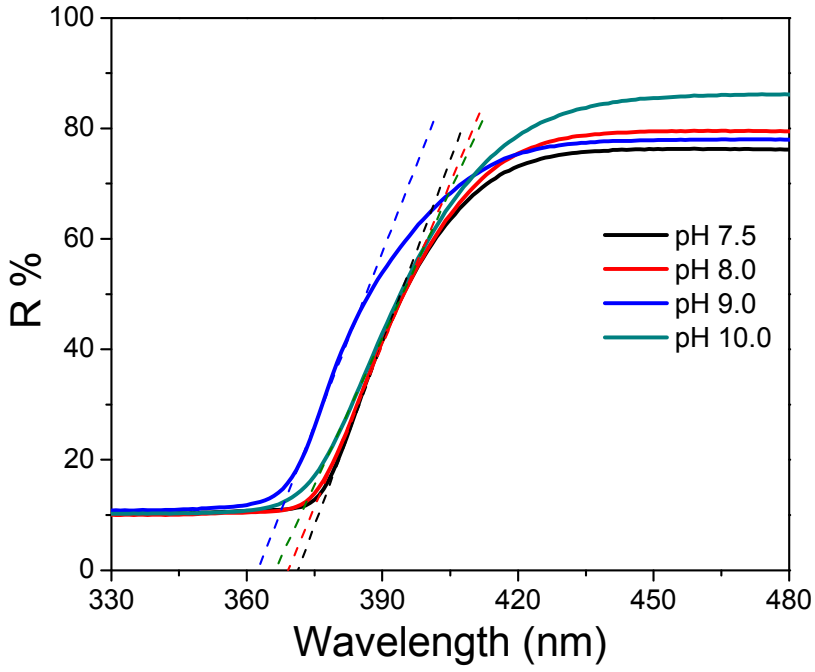

Fig. 7 DRS spectra of the as-grown ZnO nanostructures prepared at different pH values of the reaction mixture.

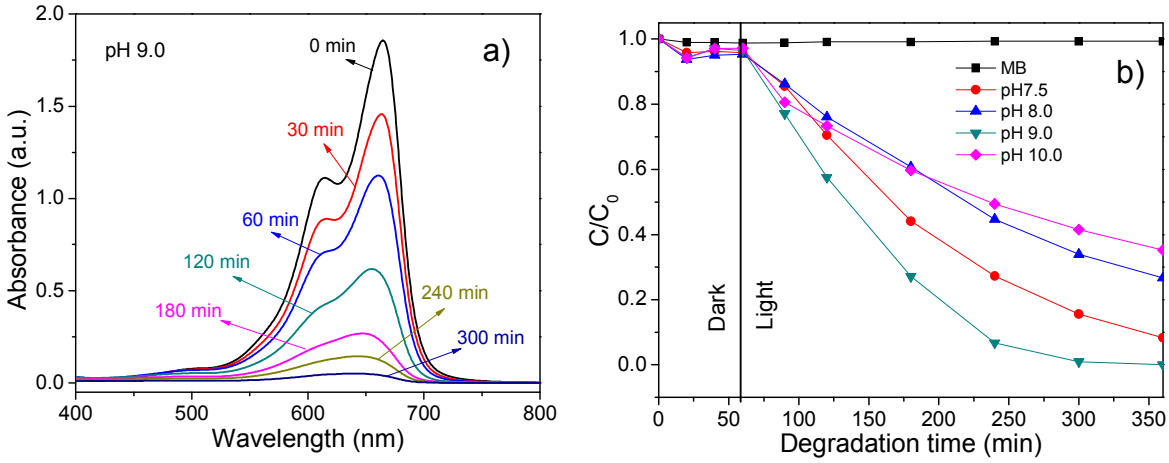

Fig. 8 a) MB absorbance spectra used to determine the photocatalytic activity of as-grown ZnO nanostructures prepared at pH 9, and b) photo-degradation rate of MB over as-grown ZnO nanostructures prepared at different pH values of the reaction mixture. The MB degradation behavior under UV illumination has also been included to show that there is no photo-degradation of MB in absence of catalyst.

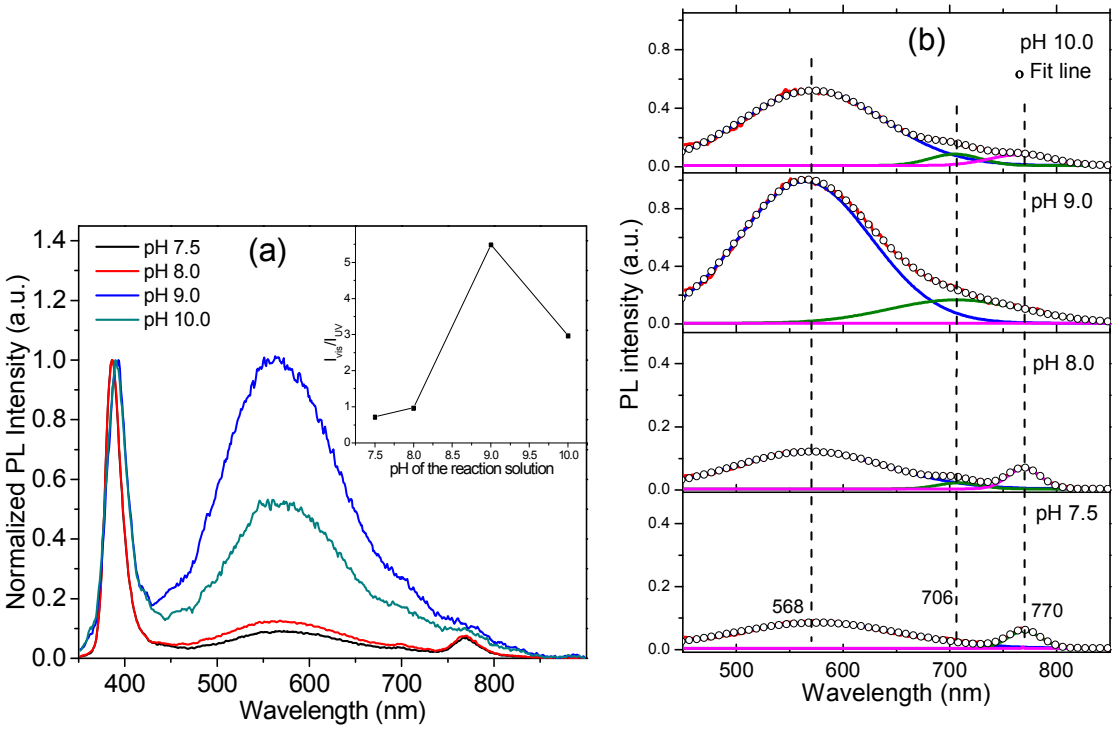

Fig. 9 (a) Room temperature PL spectra of the as-grown ZnO nanostructures prepared at different pH values of the reaction mixture. The inset shows the variation of I_{Vis}/I_{UV} intensity ratio with solution pH. (b) Gaussian deconvolution of the visible PL band for the ZnO nanostructures.

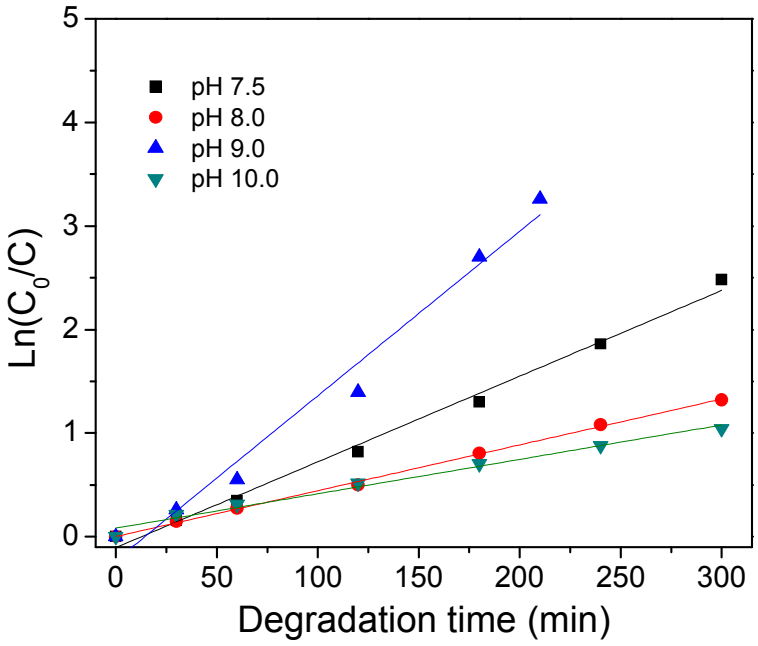

Fig. 10 Kinetic fits ($\ln(C_0/C)$ vs. time) for the photocatalytic degradation of MB by as-grown ZnO nanostructures prepared at different pH values.

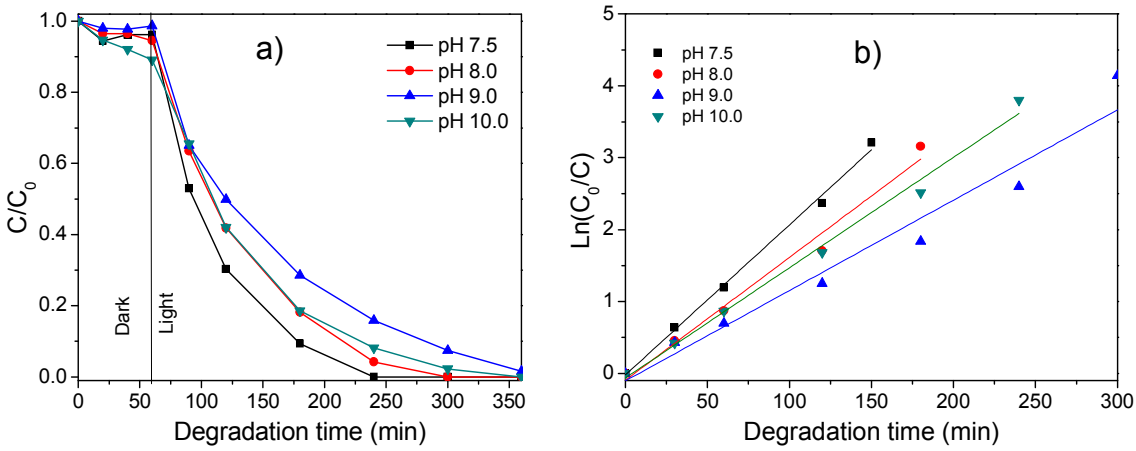

Fig. 11 a) MB photo-degradation rate by the ZnO nanostructures after thermal annealing at 525°C for 5 h in air, and b) kinetic fits ($\ln(C_0/C)$ vs. time) for the photocatalytic degradation of MB.

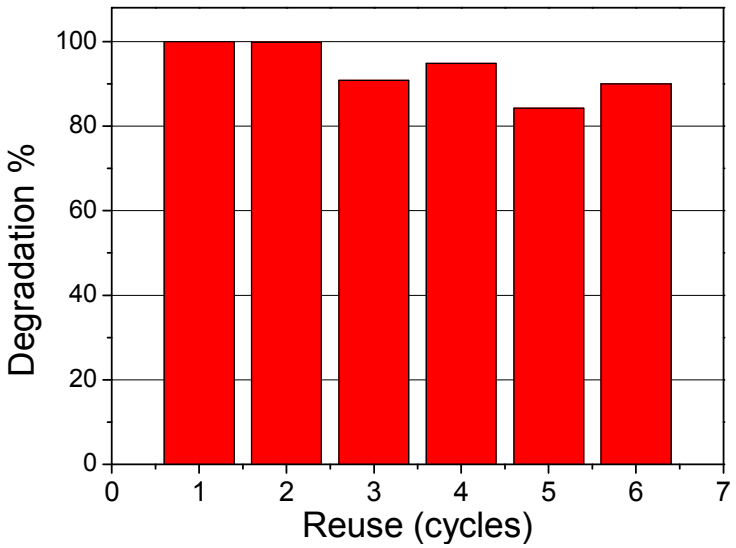

Fig. 12 Reusability test for the air-annealed ZnO nanostructures grown at pH 7.5. The estimated degradation % correspond to 180 min of degradation time.

Graphical Abstract

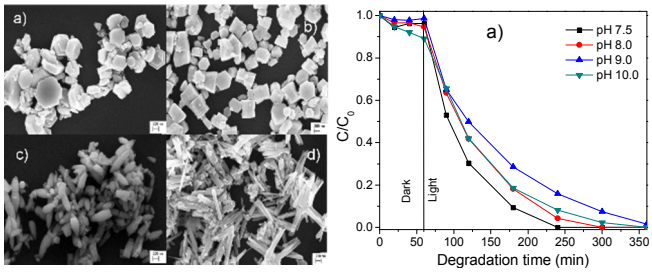

Contributions of morphology, surface area, and defect content, on the photocatalytic activity of ZnO nanostructures have been discussed.

Graphical Abstract

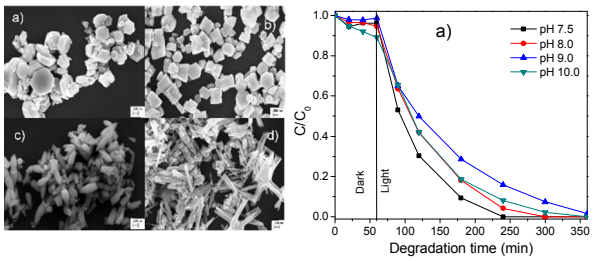

Contributions of morphology, surface area, and defect content, on the photocatalytic activity of ZnO nanostructures have been discussed.